Prediction of single-atom-thick transition metal nitride CrN$_4$ with a square-planar network and high-temperature ferromagnetism

Dapeng Liu,[1] Panjun Feng,[1] Shuo Zhang,[1] Miao Gao,[2] Fengjie Ma ◉,[3] Xun-Wang Yan ◉,[1,*] and Z. Y. Xie ◉[4,†]

[1]*College of Physics and Engineering, Qufu Normal University, Qufu, Shandong 273165, China*
[2]*Department of Physics, School of Physical Science and Technology, Ningbo University, Zhejiang 315211, China*
[3]*The Center for Advanced Quantum Studies and Department of Physics, Beijing Normal University, Beijing 100875, China*
[4]*Department of Physics, Renmin University of China, Beijing 100872, China*

Single-atom-thick two-dimensional (2D) materials such as graphene usually have a hexagonal lattice while the square-planar lattice is uncommon in the family of 2D materials. Here, we demonstrate that single-atom-thick transition metal nitride CrN$_4$ monolayer is a stable free-standing layer with a square-planar network. The stability of square-planar geometry is ascribed to the combination of N=N double bond, Cr-N coordination bond, and π-d conjugation, in which the double π-d conjugation is rarely reported in previous studies. This mechanism is entirely different from that of the reported 2D materials, leading to lower formation energy and more robust stability than the synthesized g-C$_3$N$_4$ monolayer. On the other hand, the CrN$_4$ layer has a ferromagnetic (FM) ground state, in which the FM coupling between two Cr atoms is mediated by electrons of the half-filled large π orbitals from π-d conjugation. The high-temperature ferromagnetism in CrN$_4$ monolayer is confirmed by solving the Heisenberg model with the Monte Carlo method.

I. INTRODUCTION

Two-dimensional (2D) materials possess a variety of unique electronic properties due to their reduced dimensionality, and they have attracted tremendous research interest and become focused issues of frontier research in the physics and materials fields. After graphene was discovered [1], various 2D materials have been fabricated in experiments, such as boron nitride [2], silicene [3], borophene [4], stanene [5], transition metal dichalcogenides [6], and MXenes [7].

In theoretical studies, many kinds of 2D materials have been proposed [8]. Among them, only a small fraction of 2D materials consist of a single layer of atoms such as graphene, while others consist of several atomic layers such as MoS$_2$. We call the former *single-atom-thick 2D materials*, which usually have hexagonal honeycomb geometry and are composed of group III–V elements. Because no magnetic metal element is included in these single-atom-thick 2D materials, there is no intrinsic magnetism in them, which limits their applications in magnetic devices.

Recently, the room-temperature ferromagnetism in CoN$_4$-embedded graphene was realized, and the Curie temperature reached up to 400 K, in which 3d metal Co atoms were anchored in the graphene plane by the aid of N atoms [9]. In fact, >20 kinds of metal atoms can be implanted into the graphene plane in the form of the MN$_4$ (M = metal) moiety in experiments of single-atom catalysts synthesis [10,11], and the planar geometry of MN$_4$ in graphene sheets has been ob-served by systematic x-ray absorption fine structure analyses and direct transmission electron microscopy imaging [12].

In theoretical works, the structural stability of CoN$_4$C$_{10}$, CoN$_4$C$_2$, and CrN$_4$C$_2$ monolayers consisting of MN$_4$ are demonstrated by means of first-principles calculations [13–15]. The above studies indicate that the MN$_4$ moiety is a special structural component.

A natural question is whether there is a free-standing monolayer composed of only the MN$_4$ moiety. On the other hand, another compound catches our attention. Triclinic beryllium tetranitride BeN$_4$ was synthesized under the pressure of 85 GPa very recently [16], and it transforms into layered van der Waals bonded BeN$_4$ with small exfoliation energy. The planar BeN$_4$ layer with single-atomic thickness is regarded as a class of 2D materials which is made up of only BeN$_4$ moieties linked together with a staggered alignment. The stability of the BeN$_4$ monolayer further provides powerful evidence for the high feasibility to synthesize the planar MN$_4$ (M = 3d metal) monolayer.

In a recent theoretical study, MgN$_4$, PtN$_4$, RhN$_4$, and IrN$_4$ layers with a similar structure to the BeN$_4$ monolayer were proved to be stable by first-principles calculations, while the free-standing NiN$_4$ and CuN$_4$ layers were found to be unstable [17]. Because Ref. [17] focuses on the nonmagnetic analogs of the BeN$_4$ layer, other magnetic metals such as Cr have not been considered in their work. Therefore, we want to clarify the two following questions.: One is whether the CrN$_4$ moiety can form planar single-atom-thick layers, and the other is, if so, what structure would be formed?

The reason we choose the Cr element is that Cr is a typical transition metal element, and the majority of chromium compounds are magnetic materials. Furthermore, the pla-

*Corresponding author: yanxunwang@163.com
†Corresponding author: qingtaoxie@ruc.edu.cn

nar square CrN monolayer with a ratio of Cr:N = 1:1 and
its robust ferromagnetism were predicted in the previous
study [18]. The CALYPSO package [19] is software for crystal
structure searching and has been used extensively. Using the
2D structure search function in CALYPSO, we do a structure
search with the fixed ratio of Cr:N = 1:4 (see Appendix B),
and a square CrN_4 sheet with the lowest energy is screened
out. Such a square porous network looks unexpected and has
not been reported in previous studies.

In this paper, we will focus on the distinctive square CrN_4
monolayer, demonstrate the stability, analyze the stability
mechanism, confirm the high-temperature ferromagnetism,
and uncover the origin of the ferromagnetism.

II. COMPUTATIONAL DETAILS

The calculations are performed in the VASP package, in
which the plane-wave pseudopotential method and the projec-
tor augmented-wave (PAW) pseudopotential with the Perdew-
Burke-Ernzerhof (PBE) functional [20–23] are adopted. The
nonempirical strongly constrained and appropriately normed
(SCAN) meta-generalized gradient approximation (GGA)
method, the GGA + U method, and the Heyd-Scuseria-
Ernzerhof screened hybrid functional (HSE) method are
employed to consider the correction of electron correla-
tion [24–26]. The plane-wave basis cutoff is 800 eV, and the
thresholds are 10^{-5} eV and 0.001 eV/Å for total energy and
force convergence. The interlayer distance was set to 18 Å,
and a mesh of 24 × 24 × 1 k-points is used for the Brillouin
zone integration.

The phonon calculations are carried out with the super-
cell method in the PHONOPY program, and the real-space
force constants of supercells were calculated using density
functional perturbation theory (DFPT) as implemented in
VASP [27]. The force convergence criterion (10^{-5} eV/Å) was
used in structural optimization of the primitive cell before
building the supercell. In the *ab initio* molecular dynamics
simulations, 3 × 3 × 1 supercells were employed, and the
temperature was kept at 1000 K for 10 ps with a time step of
1 fs in the canonical ensemble (NVT) [28]. The temperature
of the phase transition in the CrN_4 system is evaluated by
the Monte Carlo method enclosed in the software package
developed by Zhang *et al.* [29], and the 100 × 100 × 1 lattice
is used in the Monte Carlo simulation.

III. RESULTS AND DISCUSSIONS

A. Atomic structure and stability mechanism

The atomic structure of the square CrN_4 monolayer is
shown in Fig. 1. The basic structural unit is the CrN_4 moi-
ety, in which the Cr atom is coordinated by four N atoms
and located at the center of the N atom square. The units
are aligned with a top-and-bottom pattern and connected to
each other by N=N double bonds, forming a porous square
network. The primitive unit cell consists of one Cr atom and
four N atoms, and the lattice parameters are $a = b = 4.92$ Å.
The lengths of N-Cr and N=N double bonds are 1.88 and
1.16 Å, respectively.

What mechanism results in the stability of the square-
planar CrN_4 monolayer? The first thing we notice is the
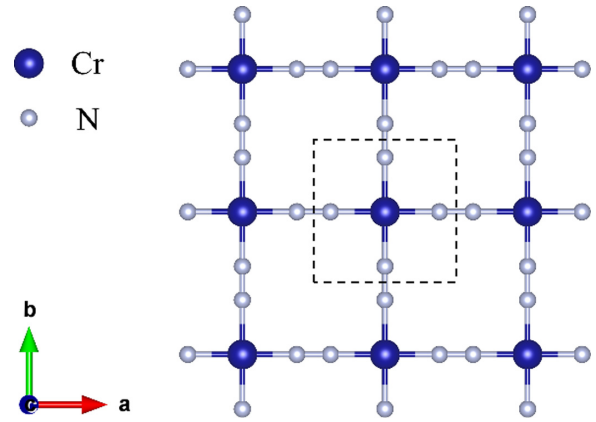
FIG. 1. Atomic structure of square CrN_4 monolayer with all
atoms in a plane. The unit cell is marked with a dashed line square.

N=N double bond between two adjacent CrN_4 units, which
is stronger and shorter than the N–N single bond because the
energy of an N=N double bond is 2.17 times that of an N–N
single bond. Through these N=N double bonds, the CrN_4
moieties are tightly and firmly linked together and make up
a stable configuration with low total energy.

The next thing to note is the N–Cr coordination bond inside
the CrN_4 moiety, in which the N atom provides a lone pair
electrons, and the Cr atom provides empty orbitals. For the Cr
atom, the $4s$, $4p_x$, $4p_y$, and $3d_{x^2-y^2}$ orbitals interact to form
four dsp^2 hybridized orbitals. This is a common situation
in phthalocyanine compounds and some 2D metal-organic
frameworks [30,31]. Apart from these, the π bond of N=N
is coupled to the Cr d_{xz}, d_{yz}, and d_{xy} orbitals to form a π-d
conjugation, which further increases the strength of Cr–N
bond, lowers the total energy, and enhances the robustness of
the planar structure.

B. Evidences of structural stability

After analyzing the bonding features in the CrN_4 layer, we
then compute the phonon dispersion and do the molecular
dynamics simulations to inspect the dynamical and thermal
stability. Figure 2 displays the phonon curves of the CrN_4
layer. Among them, three acoustic modes start from the Γ
point, and no imaginary frequency is observed. The molecular
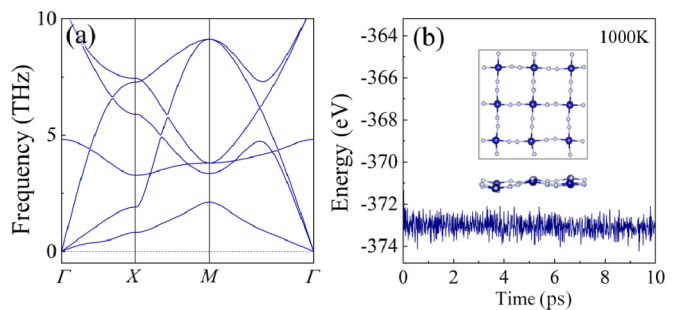
FIG. 2. (a) Phonon spectra of CrN_4 monolayer. (b) The evolution
of total potential energy with the time at 1000 K for 10 ps, where the
insets are the top and side views of the final configuration of CrN_4
monolayer after 10 ps molecular dynamics simulation.
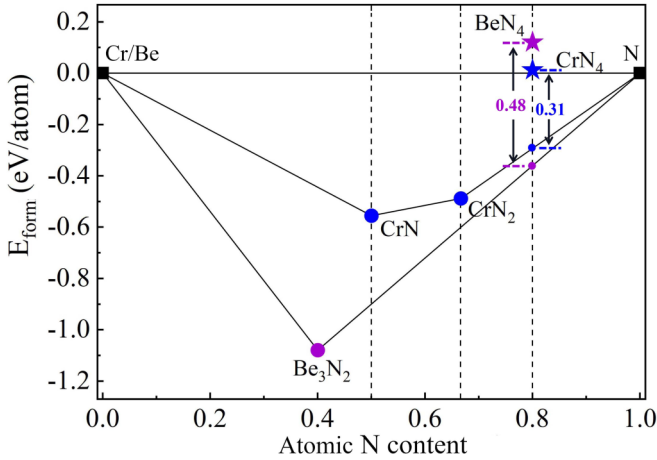
FIG. 3. The convex hull diagram of Cr–N and Be–N systems.

FIG. 4. Partial density of states of Cr $3d$ and N $2p$ suborbitals in CrN$_4$ sheet. The insets are the diagrams of the relevant orbital shape.

dynamics simulation of the CrN$_4$ layer is performed at the temperature of 1000 K for the time of 10 ps. We find that the total potential energy fluctuates around a certain value, and no distinct drop of the energy emerges. The final structure of the CrN$_4$ monolayer remains its original framework, and no bond is broken. Therefore, these results demonstrate that the CrN$_4$ monolayer has good thermal and dynamical stability.

The mechanical stability of 2D materials can also be examined by the elastic constants and Young's modulus [32]. We compute the elastic constants of the CrN$_4$ sheet, and the values of $C_{11} = C_{22} = 127.1$ N/m, $C_{12} = C_{21} = 8.7$ N/m, and $C_{66} = 2.3$ N/m are obtained. These elastic constants satisfy the two inequalities $C_{11}C_{22} - C_{12}C_{21} > 0$ and $C_{66} > 0$, namely, they satisfy the mechanical stability Born criteria [33]. According to the formulas $E_x = (C_{11}C_{22} - C_{12}C_{21})/C_{22}$ and $E_y = (C_{11}C_{22} - C_{12}C_{21})/C_{11}$, the in-plane Young;'s moduli we obtain are $E_x = E_y = 126.5$ N/m. Young's moduli of the CrN$_4$ monolayer are comparable with the ones of SiC, GeC, and BeC monolayers, which are 163.5, 140.1, and 145.54 N/m, respectively [32,34]. Hence, the CoN$_4$ monolayer is mechanically stable. The formation energy of the CrN$_4$ monolayer is computed in terms of the expression $E_{form} = \frac{1}{n}(E_{tot} - E_{metal} - 2E_{N_2})$, in which E_{tot}, E_{metal}, and E_{N_2} are the total energy, bulk metal energy per atom, and nitrogen molecule energy, respectively.

For comparison, we also compute the formation energies of g-C$_3$N$_4$ and BeN$_4$ monolayers synthesized in experiments, and they are 0.346 and 0.121 eV. The calculated formation energy of the CrN$_4$ monolayer is 0.013 eV, much smaller than the ones of g-C$_3$N$_4$ and BeN$_4$ monolayers. Figure 3 shows the binary phase diagrams of Cr–N and Be–N compounds, in which bulk CrN [35], CrN$_2$ [36], Be$_3$N$_2$ [37], metal Cr [38], metal Be [39], and gas N$_2$ make up the convex hull. The hull energy of the CrN$_4$ monolayer is 0.31 eV, less than the hull energy 0.48 eV of the BeN$_4$ monolayer. The energies of BeN$_4$ and CrN$_4$ above zero in Fig. 3 are just their formation energies of 0.121 and 0.013 eV. The formation energy and hull energy of CrN$_4$ are comparable with the ones of g-C$_3$N$_4$ and BeN$_4$ monolayers synthesized in experiments, indicating that it is highly feasible to fabricate the CrN$_4$ monolayer by
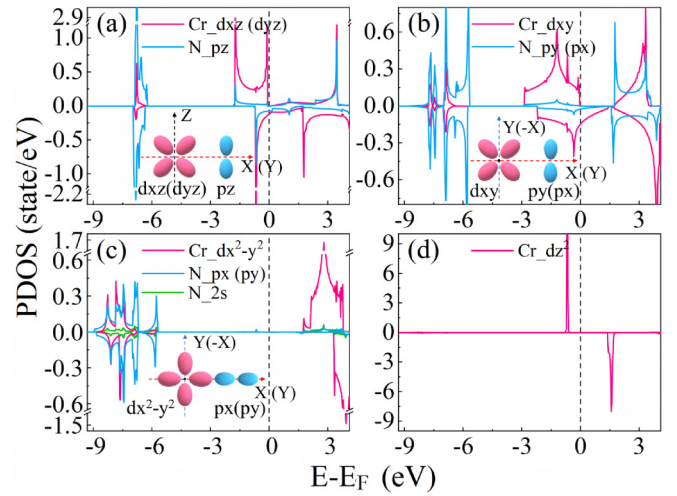
the high-pressure synthesis method, like the synthesis of the BeN$_4$ compound [16].

C. Electronic structure

Then we investigate the electronic structure of the CrN$_4$ layer. The Cr atom is located at a square plane field, whose plane symmetry is $P4m$ affiliated to point group D_4. The five partial d orbitals are divided into four groups, namely d_{xz}/d_{yz}, d_{z^2}, d_{xy}, and $d_{x^2-y^2}$. In Fig. 4(a), the partial density of states of Cr d_{xz} (d_{yz}) and N p_z orbitals are displayed, and they are distributed in the same energy range and take part in the formation of π-d conjugated electronic states.

Meanwhile, along the x (y)-axis direction, the Cr d_{xy} orbital and N p_y (p_x) make up another π-d conjugation, shown in Fig. 4(b). Namely, along the Cr–N=N–Cr chain in the x (y) direction, there are two kinds of π-d conjugations; one is related to d_{xz}-p_z-p_z-d_{xz} (d_{yz}-p_z-p_z-d_{yz}) orbitals and the other to d_{xy}-p_y-p_y-d_{xy} (d_{xy}-p_x-p_x-d_{xy}) orbitals.

Figure 4(c) displays the density of states of Cr $d_{x^2-y^2}$ and N p_x (p_y) and s orbitals. The three orbitals are related to the Cr–N coordination bond for which the $d_{x^2-y^2}$ orbital is empty and a lone pair of electrons comes from the hybridized states of N p_x (p_y) and s orbitals. The density of states of Cr d_{z^2} orbitals are presented in Fig. 4(d), and their spin-up states are fully occupied, and the spin-down states are empty. The spin polarization of electrons in d_{z^2}, d_{xz}, d_{yz}, and d_{xy} orbitals gives rise to the magnetic moment of 2 μ_B around the Cr atom.

Figures 5(a)–5(d) display the energy band structures of the CrN$_4$ monolayer in the ferromagnetic (FM) phase with PBE, GGA + U, SCAN, and HSE functional methods, respectively. The red and blue curves correspond to the spin-up and spin-down bands. In the energy range from −4 to 0 eV, the positions of red curves change obviously, which reflects the considerable influence of different functionals on electronic structure of CrN$_4$. There are two hole-type bands (blue) and one electron-type band (red) crossing the Fermi energy in Figs. 5(b) and 5(c), while only two blue curves cross the Fermi energy in Fig. 5(d), indicating the larger exchange splitting in HSE calculations than in GGA + U and SCAN calculations.
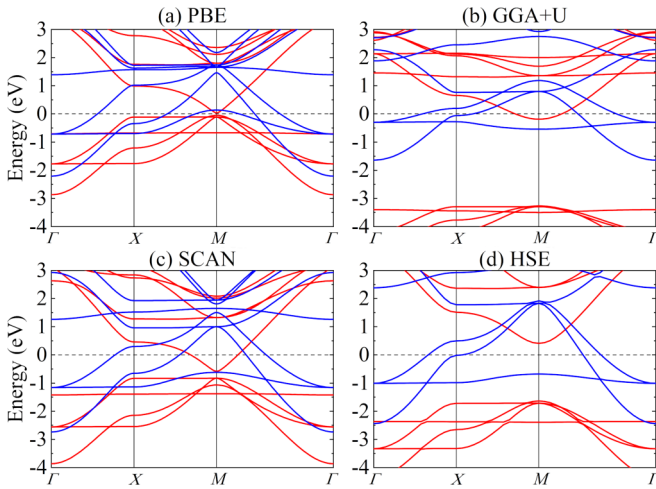
FIG. 5. Band structure of CrN_4 monolayer in ferromagnetic phase with different functional methods: (a) PBE, (b) GGA + U, (c) SCAN, (d) HSE. The Fermi energy is set to zero.

FIG. 6. (a) Top view of atomic structure of CrN_4. J_1 and J_2 are the nearest and next-nearest neighbored exchange interaction. [(b)–(d)] The sketches of FM, coll-AFM, and neel-AFM.

The metallic properties of the CrN_4 monolayer are tightly associated with these bands through the Fermi energy, which are made up of the delocalized electronic states due to the double π-d conjugation mentioned above.

The flat band is an unusual characteristic of Bloch electronic states in condensed matter physics. Due to weak dispersiveness, there are the small band width and high density of states, resulting in the small kinetic energy and large Coulomb potential energy. Because the Coulomb interaction is far greater than the kinetic energy of electrons in the flat band states, the associated compounds exhibit some exotic strong correlation phenomena, such as superconductivity [40], ferromagnetism [41], Wigner crystal [42], and the fractional quantum Hall effect [43].

A sharp peak of the density of states spectra in Fig. 4(d) is associated with the flat band around -0.7 eV below the Fermi energy in Fig. 5(a). Due to the 2D structure, there is no atom above or below the CrN_4 plane. In this special 2D crystal field, the Cr d_{z^2} orbital does not hybridize with orbitals from other atoms and keeps an isolated state, which results in the sharp peaks of density of states and the flat bands. The flat bands at -3.4 eV in Fig. 5(b), -1.4 eV in Fig. 5(c), and -2.4 eV in Fig. 5(d) all come from the d_{z^2} orbitals in the GGA + U, SCAN, and HSE functional calculations, which are closely related to the local part of the Cr moment. FM 2D materials have many potential applications in next-generation spintronic devices, but low Curie temperature is the main obstacle that hinders those applications. Therefore, exploring 2D FM materials with high critical temperature is a significant topic in physics and material fields.

D. Ferromagnetic ground state

Next, we demonstrate that the CrN_4 monolayer is a high-temperature FM monolayer. To determine the magnetic ground state of the CrN_4 monolayer, we perform the spin-polarized calculations for several magnetic orders, including the FM order, collinear antiferromagnetic (coll-AFM) order, and Néel antiferromagnetic (neel-AFM) order. The atomic
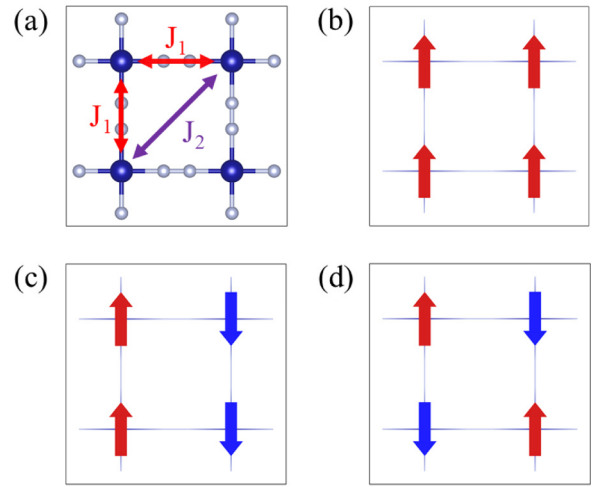
structure and three magnetic orders are sketched in Fig. 6, and for clarity, the atomic structure is displayed with the wire frame in Figs. 6(b)–6(d). To confirm the FM ground state of CrN_4, the PBE, GGA + U, SCAN, and HSE functional methods are used separately to calculate the electronic structures of the CrN_4 monolayer, and the total energies per formula cell and magnetic moments around Cr atoms are listed in Table I.

The value of Hubbard U is 5.46 eV, which is derived from the self-consistent calculation with linear response method [25]. As can be seen, the energy values from different functional methods for FM, coll-AFM, and neel-AFM states have the same order, which strongly demonstrates that the single-atom-thick CrN_4 layer is a FM 2D material. The FM coupling between two Cr moments is mediated by the N=N double bond. The physical picture is that, on the account of Hund's rule, the electron in the d_{z^2} and d_{xz} orbitals of each Cr atom has the same spin. Along a Cr–N=N–Cr chain in the x-axis direction, d_{xz}, p_z, p_z, and d_{xz} are recombined to construct the delocalized π states, and they are half-filled. Thus, the d electrons in these delocalized π states have the same spin because of Hund's rule. Consequently, d electrons in d_{xz} and d_{z^2} orbitals belonging to two Cr atoms have the same spin, and their magnetic coupling is FM. We can draw the same conclusion when the magnetic coupling is analyzed in terms of d_{yz} or d_{xy} orbitals.

The magnetic moment of the Cr atom in CrN_4 originates from the partially occupied d orbitals, shown in Fig. 4. The spin-up channel of the d_{z^2} orbital is fully occupied, and its spin-down channel is empty, which is related to the local moment of $1.0\,\mu_B$ of the Cr atom. The d_{xy}, d_{yz}, and d_{xz} orbitals distribute around the Fermi energy and make the main contribution to the metallic behavior of the CrN_4 monolayer. Each of the d_{xy}, d_{yz}, and d_{xz} orbitals provides the moment of $0.33\,\mu_B$, which corresponds to the itinerant part of the Cr moment. Thus, there are both localized and itinerant moments in the CrN_4 monolayer. Just as the Heisenberg model is used for FeSe and FeTe compounds [44,45], we use the Heisenberg model to describe the magnetic interactions in the CrN_4 layer.

TABLE I. The energies in FM, coll-AFM, and neel-AFM orders, local magnetic moment, exchange coupling J_1 and J_2, the estimated Curie temperatures (T_{c0} and T_{c1}) in terms of $J_1 2/\ln(1 + \sqrt{2})$ and the expression of Torelli and Olsen [50], and the calculated Curie temperature (T_c) by the Monte Carlo method.

Method	E_{FM} (meV)	E_{coll} (meV)	E_{neel} (meV)	Moment (μ_B)	J_1 (meV/S^2)	J_2 (meV/S^2)	A (meV/S^2)	T_{c0} (K)	T_{c1} (K)	T_c (K)
PBE	0.0	34.4	46.8	2.0	−11.7	−2.7	−0.303	309	47	121
GGA + U	0.0	115.0	124.7	2.1	−31.2	−13.2	−0.164	822	91	356
SCAN	0.0	88.8	143.4	2.0	−35.8	−4.3	−0.215	944	94	300
HSE	0.0	197.8	209.8	2.0	−52.6	−23.2	−0.291	1382	144	620

The Hamiltonian is defined as

$$H = J_1 \sum_{\langle ij \rangle} \vec{S}_i \cdot \vec{S}_j + J_2 \sum_{\langle ij' \rangle} \vec{S}_i \cdot \vec{S}_{j'} + A \sum_i (S_{iz})^2, \quad (1)$$

where j and j' denote the nearest and next-nearest neighbors of the i site. Here, J_1 and J_2 are the nearest and next-nearest neighbored couplings, which can be derived from the energy differences among FM, coll-AFM, and neel-AFM orders [46]. Also, A is the single-site magnetic anisotropic energy, which is the energy difference when the Cr moment is along (1 0 0) and (0 0 1) directions. The relevant data are shown in Table I. For the CrN$_4$ monolayer, the next-next-neighbor coupling J_3 is almost zero according to the SCAN calculations. Thus, the J_3 and other couplings over a longer distance are not contained in the Heisenberg Hamiltonian in Eq. (1). The computational details concerning J_3 are attached in Appendix A.

E. Curie temperature

The Curie temperature is a key parameter to determine the practical value of the magnetic materials. Firstly, we make a rough estimate in terms of the formula $T_c = J_1 2/\ln(1 + \sqrt{2})$ [47–49]. The analytical solution of the Ising model for a 2D square lattice, and the calculated Curie temperature (T_{c0}) are listed in Table I. Because the Ising model is the limit of the Heisenberg model with magnetic anisotropy going to infinity and the magnetic anisotropy is small in most 2D materials, the critical temperature is usually overestimated. For a magnetic 2D lattice, the Heisenberg model is a more suitable model to determine the critical temperature, in which magnetic anisotropy is essential in terms of the Mermin-Wagner theorem. Torelli and Olsen [50] proposed an analytical expression on the critical temperature by fitting the results of Monte Carlo simulations, $T_c = T_{c0}\tanh^{1/4}[\frac{6}{N_{nn}}\log(1 + \frac{0.033A}{J})]$, where N_{nn} is the number of nearest neighbors, T_{c0} is the critical temperature for the corresponding Ising model, and A and J are the single-ion magnetic anisotropy and the nearest neighboring exchange coupling, respectively. The critical temperatures obtained from the expression of Torelli and Olsen [50] are listed as T_{c1} in Table I, which are underestimated because only the nearest exchange coupling J_1 is included. Zhang *et al.* [29] developed a software package to compute the critical temperature of a 2D magnetic lattice on the base of the Heisenberg model and the Monte Carlo method, which is greatly successful in estimating the Curie temperature of the FM CrI$_3$ monolayer. By means of the software package of Zhang *et al.* [29], we solve the Heisenberg model with

the parameters J_1, J_2, and A in Table I. The variations of magnetization (M) and susceptibility ($\chi = \frac{\langle \bar{M}^2 \rangle - \langle \bar{M} \rangle^2}{k_B T}$) with respect to temperature are presented in Fig. 7, and the Curie temperatures (T_c) of the CrN$_4$ monolayer are 121, 356, 300, and 620 K according to the PBE, GGA + U, SCAN, and HSE functional methods, respectively.

The Curie temperature T_c from the HSE hybrid functional calculations is obviously higher than the ones from PBE, GGA + U, and SCAN calculations. The reason is that the HSE hybrid functional method tends to overestimate the exchange splitting of d electronic states and results in an increase of the spin-polarization energy due to the introduction of a fixed portion of the Fock exchange [51]. On the other hand, because the electronic correlation effect is not fully considered in the PBE functional, T_c according to the standard PBE calculations is usually underestimated. In the GGA + U and SCAN calculations, the electron correlation effect is more reasonably considered, which leads to the more credible Curie temperatures. This is verified by the fact that T_c of 356 and 300 K from the GGA + U and SCAN calculations are roughly consistent and can confirm each other. At present, the reported 2D FM materials usually have a low Curie temperature. As displayed in the recent review paper [52], among 44 kinds of FM 2D materials, the highest Curie temperature predicted on the basis of the Heisenberg model is 261 K. Thus, 356 and 300 K are
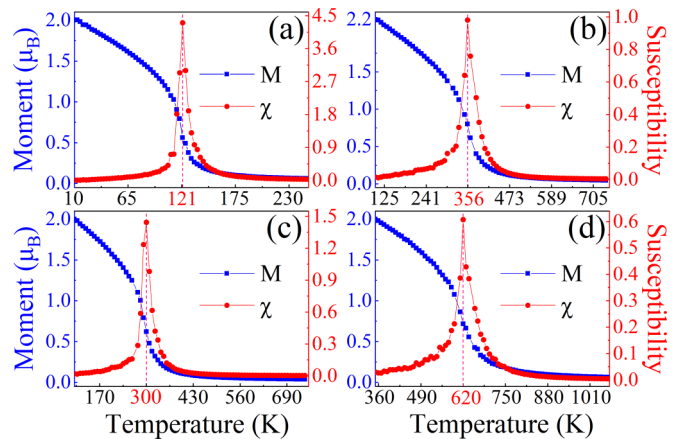
FIG. 7. The susceptibility χ and average magnetic moment M as functions of temperature for the Heisenberg model on a square lattice, and the parameters J_1, J_2, and A of the Heisenberg model derived from the various functional calculations: (a) PBE, (b) GGA + U, (c) SCAN, and (d) HSE.

TABLE II. The energies per CrN_4 formula cell in various magnetic orders and the exchange couplings J_1, J_2, and J_3. The units of energy and exchange coupling are meV and meV/S^2. The energy in FM order is set to zero.

Method	E_{FM} (meV)	E_{AFMI} (meV)	E_{AFMII} (meV)	E_{AFMIII} (meV)	J_1 (meV/S^2)	J_2 (meV/S^2)	J_3 (meV/S^2)
GGA + U	0.0	114.97	124.74	88.25	−31.2	−13.2	−11.6
SCAN	0.0	88.82	143.40	59.30	−35.8	−4.3	−0.08

high Curie temperatures for a 2D FM material. As for the mechanism of high-temperature ferromagnetism, it is closely associated with the special Cr–N=N–Cr chain of the CrN_4 monolayer, along which the double π-d conjugation can give rise to the strong exchange coupling between two neighboring Cr atoms, leading to robust ferromagnetism. The robust ferromagnetism and specific structure make the single-atom-thick CrN_4 monolayer unusual, and further study is expected.

IV. CONCLUSION

In summary, we propose a single-atom-thick 2D compound CrN_4 from first-principles calculations, which is a transition metal nitride sheet with a square-planar network structure rarely reported before. The stability has been verified by the calculations involved in phonon spectra, molecular dynamics simulation, elastic constant, and formation energy, and the mechanism is ascribed to the cooperation of the N=N double bond, the Cr–N coordination bond, and the π-d conjugation effect. The feasibility of fabrication in experiments is explained by the very small formation energy and the MN_4 (M = metal) structure units. More importantly, the CrN_4 monolayer is a FM 2D compound with a high Curie temperature.

APPENDIX A: NEXT-NEXT NEIGHBOR EXCHANGE COUPLING J_3

We compute the next-next-neighbor exchange coupling J_3 with GGA + U and SCAN methods, listed in Table II (the results from GGA + U and SCAN calculations are more credible, which has been discussed). As can be seen, J_3 from SCAN calculations almost decays to zero, and J_3 from GGA + U calculations is also less than J_2, showing an obvious decay. For the GGA + U results, when J_3 is included in the Heisenberg Hamiltonian, the Curie temperature must be higher than T_c = 356 K, presented in Table I. Therefore, the Heisenberg Hamiltonian with only J_1 and J_2 considered is reliable. For computing the next-next-neighbor exchange coupling J_3, the four magnetic orders are adopted and shown in Fig. 8.

APPENDIX B: STRUCTURAL SEARCH FOR CrN_4

The CALYPSO code is employed to confirm the square structure of the CrN_4 monolayer. Using the 2D structure search

FIG. 8. (a)Atomic structure of CrN_4 monolayer with the exchange coupling J_1, J_2, and J_3. (b) Ferromagnetic order (FM). (c) Antiferromagnetic order I (AFMI). (d) Antiferromagnetic order II (AFMII). (e) Antiferromagnetic order III (AFMIII).
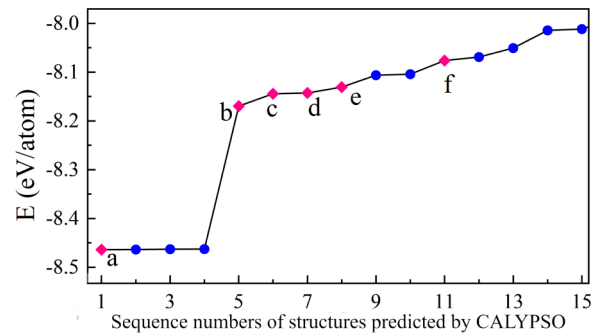
FIG. 9. Sequence numbers of structures predicted by CALYPSO. The red symbols represent the typical structures, and the blue symbols mean the repetitive one to the structure represented by the left red symbol.
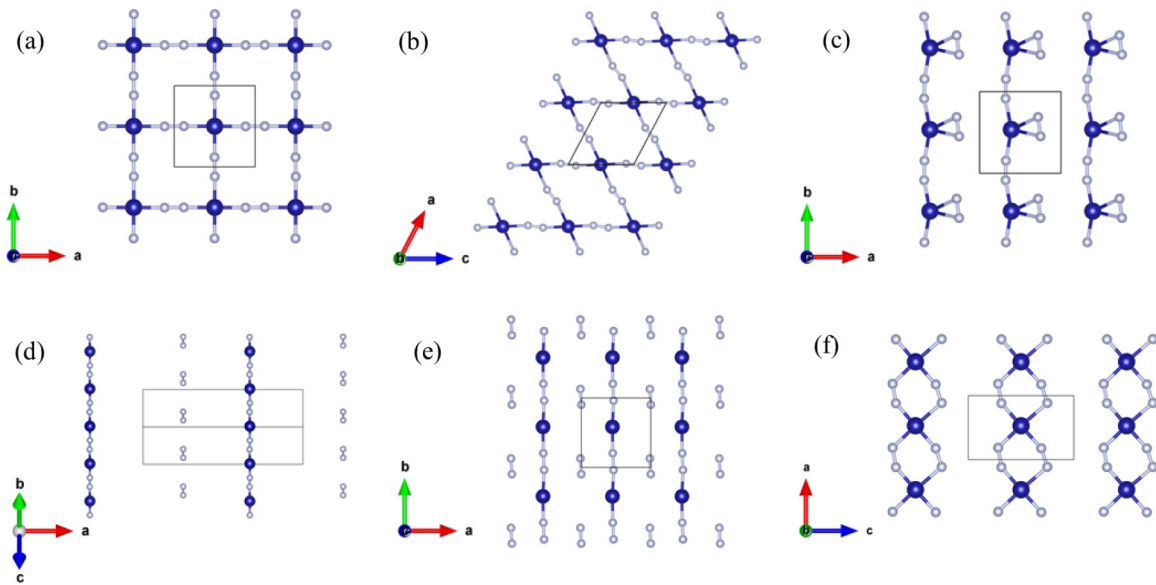
FIG. 10. The typical structures predicted by CALYPSO, the energies of which are displayed in Fig. 9 with red symbols.

function in CALYPSO, we do a structure search with the fixed ratio of Cr:N = 1:4. In Fig. 9, the horizontal axis is the sequence numbers of structures predicted by CALYPSO, and the vertical axis is the energies of different structures. The red symbols represent the typical structures, and the blue symbols mean the repetitive one to the structure represented by the left red symbol. Figure 10 displays the typical structures predicted

which are marked (a)–(f) in Fig. 9. The results demonstrate the CrN_4 monolayer in this paper is the lowest energy structure. Except the (f) structure, these structures contain the Cr–N=N–Cr chain, which indicates that the Cr–N=N–Cr chain is a low-energy structural unit. It also explains why the CrN_4 monolayer composed of Cr–N=N–Cr chains has the lowest energy.

[1] K. S. Novoselov, A. K. Geim, S. V. Morozov, D. Jiang, Y. Zhang, S. V. Dubonos, I. V. Grigorieva, and A. A. Firsov, Science **306**, 666 (2004).

[2] L. Song, L. Ci, H. Lu, P. B. Sorokin, C. Jin, J. Ni, A. G. Kvashnin, D. G. Kvashnin, J. Lou, B. I. Yakobson *et al.*, Nano Lett. **10**, 3209 (2010).

[3] B. Lalmi, H. Oughaddou, H. Enriquez, A. Kara, S. Vizzini, B. Ealet, and B. Aufray, Appl. Phys. Lett. **97**, 223109 (2010).

[4] A. J. Mannix, X.-F. Zhou, B. Kiraly, J. D. Wood, D. Alducin, B. D. Myers, X. Liu, B. L. Fisher, U. Santiago, J. R. Guest *et al.*, Science **350**, 1513 (2015).

[5] S. Saxena, R. P. Chaudhary, and S. Shukla, Sci. Rep. **6**, 31073 (2016).

[6] J. N. Coleman, M. Lotya, A. O'Neill, S. D. Bergin, P. J. King, U. Khan, K. Young, A. Gaucher, S. De *et al.*, Science **331**, 568 (2011).

[7] M. Naguib, M. Kurtoglu, V. Presser, J. Lu, J. Niu, M. Heon, L. Hultman, Y. Gogotsi, and M. W. Barsoum, Adv. Mater. **23**, 4248 (2011).

[8] M. Ashton, J. Paul, S. B. Sinnott, and R. G. Hennig, Phys. Rev. Lett. **118**, 106101 (2017).

[9] W. Hu, C. Wang, H. Tan, H. Duan, G. Li, N. Li, Q. Ji, Y. Lu, Y. Wang *et al.*, Nat. Commun. **12**, 1854 (2021).

[10] X. He, Q. He, Y. Deng, M. Peng, H. Chen, Y. Zhang, S. Yao, M. Zhang, D. Xiao, D. Ma *et al.*, Nat. Commun. **10**, 3663 (2019).

[11] W. H. Lai, H. Wang, L. Zheng, Q. Jiang, Z. C. Yan, L. Wang, H. Yoshikawa, D. Matsumura, Q. Sun, Y. X. Wang *et al.*, Angew. Chem. Int. Ed. **59**, 22171 (2020).

[12] H. Fei, J. Dong, Y. Feng, C. S. Allen, C. Wan, B. Volosskiy, M. Li, Z. Zhao, Y. Wang *et al.*, Nat. Catal. **1**, 63 (2018).

[13] D. Liu, S. Zhang, M. Gao, and X.-W. Yan, Phys. Rev. B **103**, 125407 (2021).

[14] D. Liu, P. Feng, M. Gao, and X.-W. Yan, Phys. Rev. B **103**, 155411 (2021).

[15] D. Liu, S. Zhang, M. Gao, X.-W. Yan, and Z. Y. Xie, Appl. Phys. Lett. **118**, 223104 (2021).

[16] M. Bykov, T. Fedotenko, S. Chariton, D. Laniel, K. Glazyrin, M. Hanfland, J. S. Smith, V. B. Prakapenka, M. F. Mahmood, A. F. Goncharov *et al.*, Phys. Rev. Lett. **126**, 175501 (2021).

[17] B. Mortazavi, F. Shojaei, and X. Zhuang, Mater. Today Nano **15**, 100125 (2021).

[18] S. Zhang, Y. Li, T. Zhao, and Q. Wang, Sci. Rep. **4**, 5241 (2015).

[19] C. Tang, G. Kour, and A. Du, Chin. Phys. B **28**, 107306 (2019).

[20] G. Kresse and J. Hafner, Phys. Rev. B **47**, 558 (1993).

[21] G. Kresse and J. Furthmüller, Phys. Rev. B **54**, 11169 (1996).

[22] J. P. Perdew, K. Burke, and M. Ernzerhof, Phys. Rev. Lett. **77**, 3865 (1996).

[23] P. E. Blöchl, Phys. Rev. B **50**, 17953 (1994).

[24] J. Sun, A. Ruzsinszky, and J. P. Perdew, Phys. Rev. Lett. **115**, 036402 (2015).

[25] M. Cococcioni and S. de Gironcoli, Phys. Rev. B **71**, 035105 (2005).

[26] A. V. Krukau, O. A. Vydrov, A. F. Izmaylov, and G. E. Scuseria, J. Chem. Phys. **125**, 224106 (2006).

[27] A. Togo and I. Tanaka, Scr. Mater. **108**, 1 (2015).

[28] G. J. Martyna, M. L. Klein, and M. Tuckerman, J. Chem. Phys. **97**, 2635 (1992).

[29] Y. Zhang, B. Wang, Y. Guo, Q. Li, and J. Wang, Comput. Mater. Sci. **197**, 110638 (2021).

[30] F. X. Sauvage, M. G. De Backer, and B. Stymne, Spectroch. Acta A **38**, 803 (1982).

[31] M. Wang, R. Dong, and X. Feng, Chem. Soc. Rev. **50**, 2764 (2021).

[32] R. C. Andrew, R. E. Mapasha, A. M. Ukpong, and N. Chetty, Phys. Rev. B **85**, 125428 (2012).

[33] M. Born and K. Huang, *Dynamical Theory of Crystal Lattices* (Clarendon Press, Oxford, 1954).

[34] C.-S. Liu, H.-H. Zhu, X.-J. Ye, and X.-H. Yan, Nanoscale **9**, 5854 (2017).

[35] P. Ettmayer, W. Schebesta, A. Vendl, and R. Kieffer, Monatsh. Chem. **109**, 929 (1978).

[36] K. Niwa, T. Yamamoto, T. Sasaki, and M. Hasegawa, Phys. Rev. Mater. **3**, 053601 (2019).

[37] O. Reckeweg, C. Lind, A. Simon, and F. J. DiSalvo, Z. Naturforsch. B **58**, 159 (2003).

[38] A. J. Bradley and E. F. Ollard, Nature (London) **117**, 122 (1926).

[39] A. Martin and A. Moore, J. Less Comm. Met. **1**, 85 (1959).

[40] S. Miyahara, S. Kusuta, and N. Furukawa, Phys. C **460-462**, 1145 (2007).

[41] S. Zhang, H.-h. Hung, and C. Wu, Phys. Rev. A **82**, 053618 (2010).

[42] C. Wu, D. Bergman, L. Balents, and S. Das Sarma, Phys. Rev. Lett. **99**, 070401 (2007).

[43] T. Neupert, L. Santos, C. Chamon, and C. Mudry, Phys. Rev. Lett. **106**, 236804 (2011).

[44] F. Ma, W. Ji, J. Hu, Z.-Y. Lu, and T. Xiang, Phys. Rev. Lett. **102**, 177003 (2009).

[45] R. Yu and Q. Si, Phys. Rev. Lett. **115**, 116401 (2015).

[46] F. Ma, Z.-Y. Lu, and T. Xiang, Phys. Rev. B **78**, 224517 (2008).

[47] L. Onsager, Phys. Rev. **65**, 117 (1944).

[48] H.-C. Yang, B.-C. Gong, K. Liu, and Z.-Y. Lu, Sci. Bull. **63**, 887 (2018).

[49] Z. Y. Xie, J. Chen, M. P. Qin, J. W. Zhu, L. P. Yang, and T. Xiang, Phys. Rev. B **86**, 045139 (2012).

[50] D. Torelli and T. Olsen, 2D Mater. **6**, 015028 (2019).

[51] J. Paier, M. Marsman, K. Hummer, G. Kresse, I. C. Gerber, and J. G. Ángyán, J. Chem. Phys. **124**, 154709 (2006).

[52] Y. Guo, B. Wang, X. Zhang, S. Yuan, L. Ma, and J. Wang, InfoMat **2**, 639 (2020).